Supplementary Information

Interfacial charge transfer-mediated Fermi level pinning in MBE-grown 2D 2H-$MoSe_2$/2H-$MoTe_2$ heterostructure

Kamlesh Bhatt, Santanu Kandar, Lipika, Ashok Kapoor, and Rajendra Singh*

Department of Physics, Indian Institute of Technology Delhi, Hauz Khas, New Delhi 110016, India.

**E-mail: rsingh@physics.iitd.ac.in*

Fig. S1

Raman mapping has been performed over a 20 × 20 μm^2 area across the lateral edge of the $MoSe_2/MoTe_2$ heterostructure to confirm phase uniformity. The two-dimensional intensity maps of the characteristic Raman modes for $MoSe_2$ and $MoTe_2$ are presented in Fig. a, b. The Raman maps show uniform intensity distribution across the right side of the edge for MoSe2, and across the entire region for the underlying $MoTe_2$, confirming consistent phase uniformity. Minor variations observed in some regions for $MoTe_2$ are likely due to overcorrection of the background during batch plotting, since the Raman signal of $MoTe_2$ is much weaker than that of $MoSe_2$, and also both lie at a small energy difference. To further confirm large-area phase uniformity, we also acquired Raman spectra from multiple locations across the heterostructure (Fig.c), all of which consistently show the presence of the 2H phase of MoTe2 and MoSe2 at the respective probed locations (Fig. d).

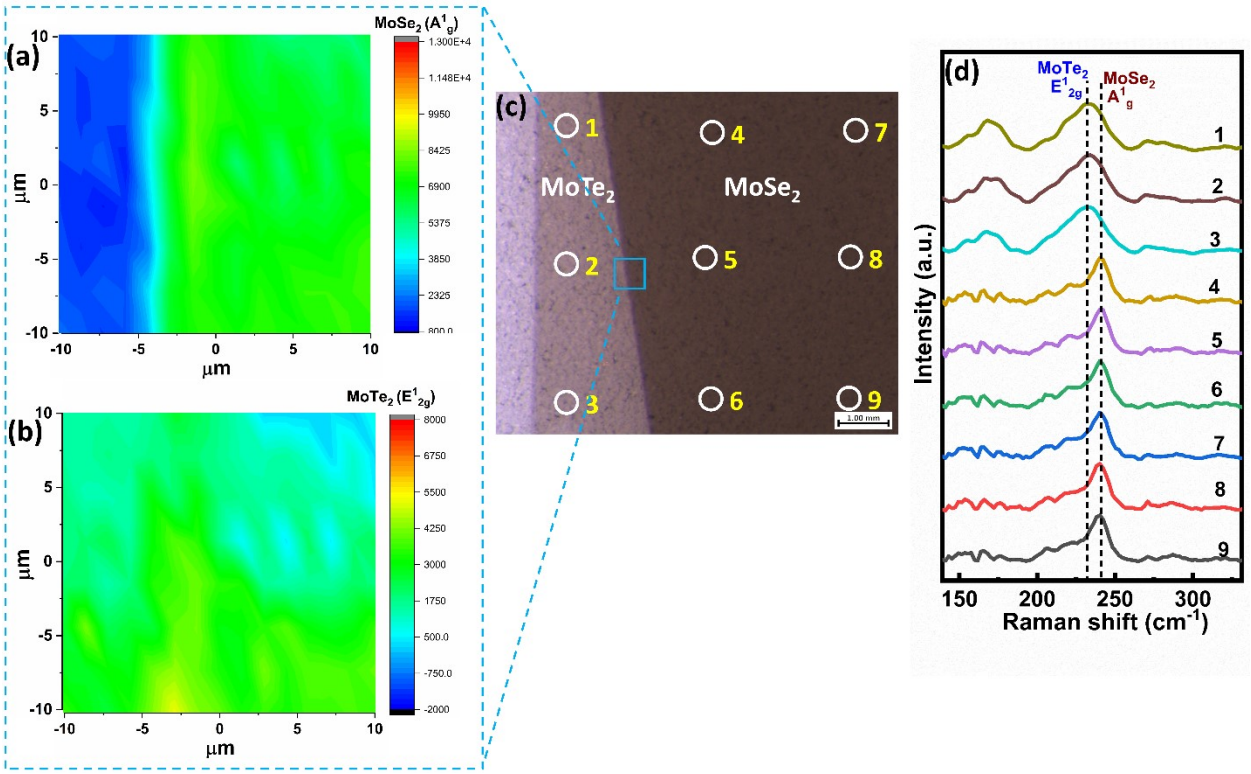

Fig. S1 Raman mapping and spectra of the $MoSe_2/MoTe_2$ heterostructure. (a) Raman intensity map of the $MoSe_2$ A^1_g mode, and (b) the $MoTe_2$ E^1_{2g} mode. (c) Optical microscope image of the heterostructure with marked positions corresponding to approximate Raman spectra acquisition points across the heterostructure. (d) Raman spectra recorded at the marked positions, showing the characteristic peaks of $MoTe_2$ and $MoSe_2$.

Fig. S2

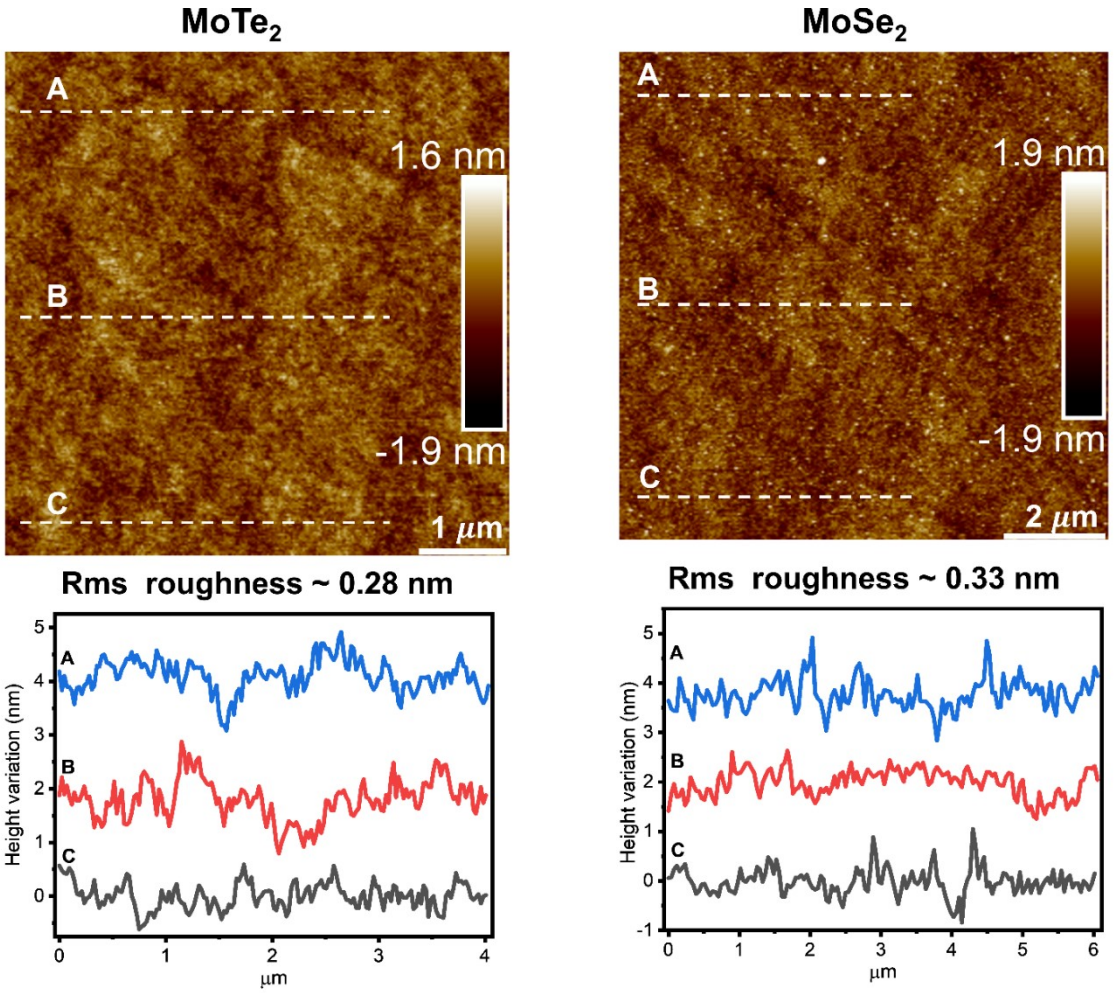

Fig. S2 AFM images of $MoTe_2$ and $MoSe_2$, with multiple line profiles across the surface, reflecting smooth film sufaces with low surface roughnesses of 0.28 nm and 0.33 nm, respectively.

Fig. S3

The precise value of the valence band edge is calculated by fitting the VB edge using the Edge down function in the casaXPS software. The Edge down function gives a more accurate result than simple linear extrapolation, as it models the band edge onset using a complementary error function, which is the convolution of the intrinsic step edge and the Gaussian broadening around the edge. The Edge down fitting graphs from casaXPS are also included in this figure.

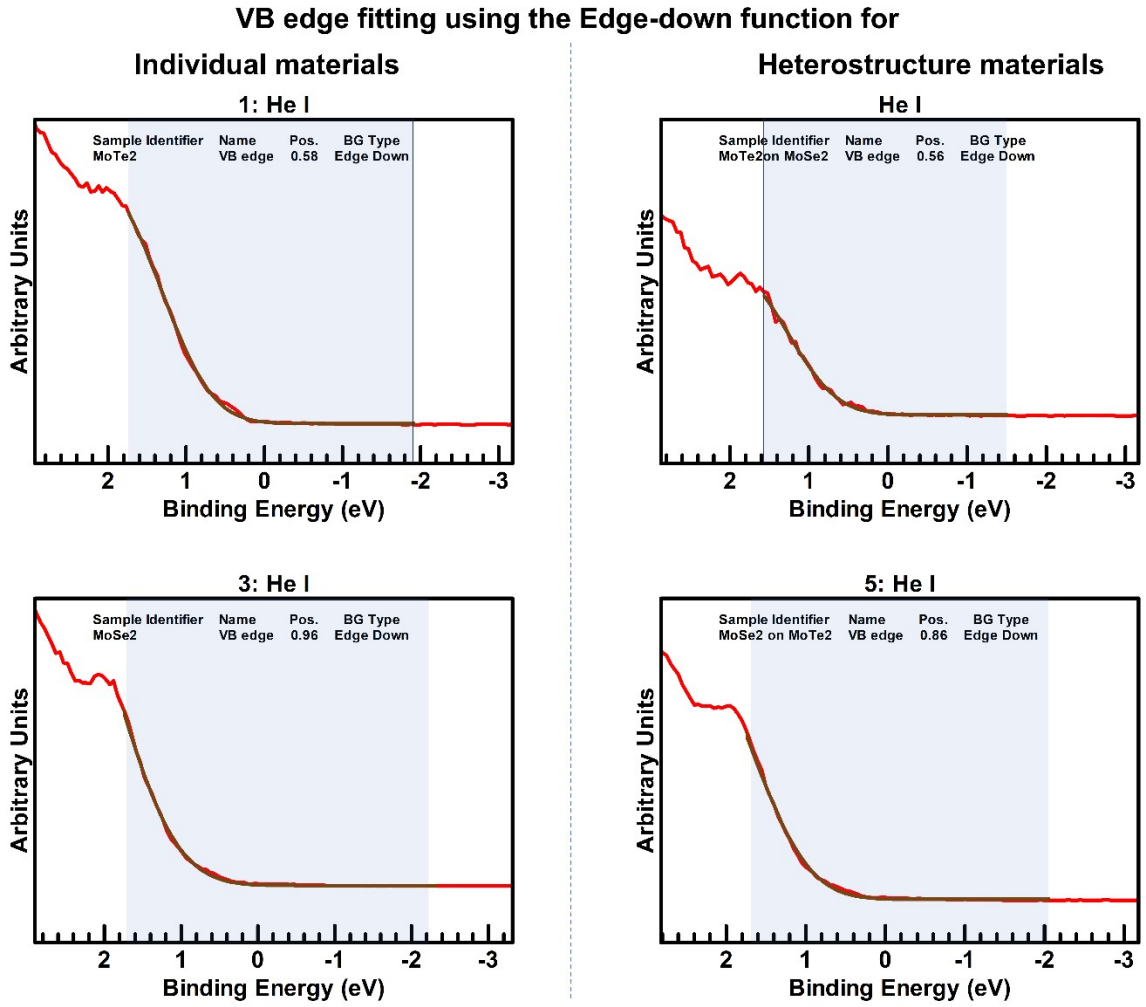

Fig. S3 The UPS spectra for individual materials, MoTe2, MoSe2 and for heterostructures are presented from the casaXPS interface. The graphs show the fitting of the valence band edge using the Edge down function for calculating the position of the band edge, where the shaded region corresponds to the fitted region of the spectrum.

Fig. S4

The AR-XPS performed at 60° emission angle (Fig. S4a) shows that the relative contribution from different bonding states of Mo, Te and Se does not show any significant variation in comparison to that for the normal emission, as shown in Fig. 5c. For 20° emission angle, the collected signal is very weak at such a small emission angle with a poor resolution of the recorded spectra; hence the spectral fitting lacks reliability and we avoid drawing any conclusions based on this.

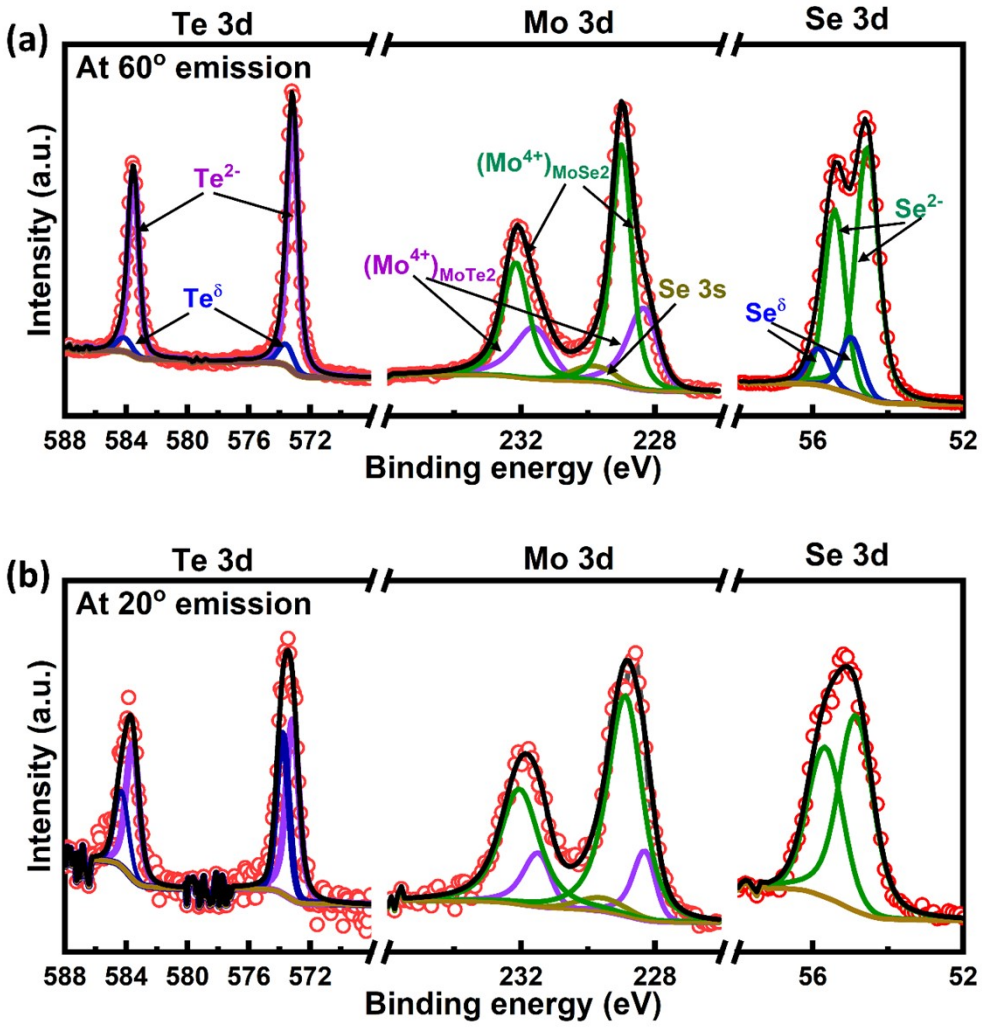

Fig. S4 AR-XPS core level spectra of Te 3d, Mo 3d and Se 3d, taken at (a) 60° emission angle, and (b) 20 ° emission angle

Fig. S5

The density functional theory (DFT) calculations are carried out to simulate Te-vacancy defect states in $MoTe_2$. Figure shows the resulting density of states (DOS) spectra for $MoTe_2$ with and without Te vacanacy. The DOS spectra shows that Te vacancies in $MoTe_2$ introduce prominent localized states just below the conduction band minimum.

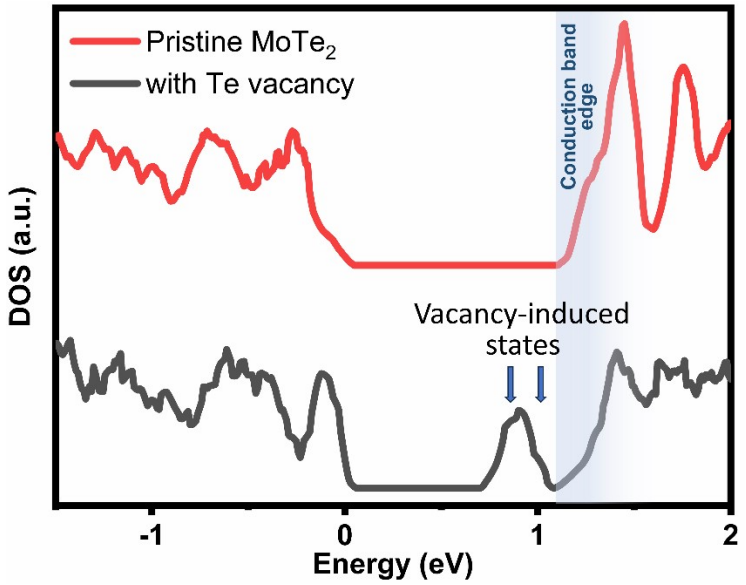

Fig. S5 Density of states (DOS) spectra of pristine $MoTe_2$ (red) and $MoTe_2$ with Te vacancies (black). The presence of Te vacancies induces localized defect states just below the conduction band minimum.

Table S1

To support these observations and quantify the thermodynamic favorability of Te vacancy formation, we calculated vacancy formation energies for Te and Mo in $MoTe_2$ and for Se vacancy in $MoSe_2$ using DFT. The vacancy formation energy (for example, for Te vacancy) was obtained using the relation:

$$E_f(V_{Te}) = E(total\ with\ V_{Te}) - E(total\ for\ pristine) + \mu_{Te}$$

where $E(total\ with\ V_{Te})$ is the total energy of the supercell containing the vacancy, $E(total\ for\ pristine)$ is the energy of the pristine supercell without any vacancy and μ_{Te} is the chemical potential of the removed atom (here Te). The calculations reveal that Te vacancies are the favorable intrinsic defect in $MoTe_2$, having a lower vacancy formation energy than that for Mo vacancies.

Table S1. Vacancy formation energies of Te and Mo in $MoTe_2$, and Se vacancies in $MoSe_2$, calculated using DFT under atomic rich conditions.

Vacancy type	**Te vacancy**	**Mo vacancy**	**Se vacancy**
E (total for pristine)$_{MoTe2\ or\ MoSe2}$	− 303.24 eV	− 303.24 eV	− 333.10 eV
E (total with vacancy)	− 297.16 eV	− 288.90 eV	− 326.28 eV
Chemical potential per atom (μ_{Te} or μ_{Mo} or μ_{Se})	− 3.44 eV	− 11.45 eV	− 3.72 eV
Formation energy (E_f)	2.64 eV	2.89 eV	3.10 eV

Table S2

Table S2. XPS peak fitting parameters of different deconvoluted components for individual materials $MoTe_2$, $MoSe_2$ and $MoSe_2/MoTe_2$ heterostructure.

Material	Core level	Bonding elements	Component	Line shape	Binding Energy (eV)	FWHM (eV)	Peak area (CPSeV)
$MoTe_2$	Mo 3d	Mo-Te	3d 5/2 (Mo^{4+})	LA(1.3,2.44,69)	228.32	0.66	2254
		Mo-Te	3d 3/2 (Mo^{4+})	LA(1.3,2.44,69)	231.51	0.91	1634
	Te 3d	Mo-Te	3d 5/2 (Te^{2-})	LA(85)	573.15	0.87	12884
		Mo-Te	3d 3/2 (Te^{2-})	LA(80)	583.52	0.87	8257
$MoSe_2$	Mo 3d	Mo-Se	3d 5/2 (Mo^{4+})	LA(1.33,1.55,69)	229.06	0.65	5478
		Mo-Se	3d 3/2 (Mo^{4+})	LA(1.33,1.25,69)	232.21	0.89	3747
	Se 3s	Mo-Se	3s	LA(50)	230.10	1.75	718
	Se 3d	Mo-Se	3d 5/2 (Se^{2-})	LA(80)	54.73	0.66	2920
		Mo-Se	3d 3/2 (Se^{2-})	LA(10)	55.58	0.72	1815
$MoSe_2$/ $MoTe_2$	Mo 3d	Mo-Te	3d 5/2 (Mo^{4+})	LA(1.3,2.44,69)	228.27	0.92	4540
		Mo-Te	3d 3/2 (Mo^{4+})	LA(1.3,2.44,69)	231.44	1.18	2853
		Mo-Se	3d 5/2 (Mo^{6+})	LA(1.33,1.55,69)	229.18	0.62	6557
		Mo-Se	3d 3/2 (Mo^{6+})	LA(1.33,1.25,69)	232.32	0.84	4680
	Se 3s	Mo-Se	3s	LA(50)	230.05	1.18	1226
	Te 3d	Mo-Te	3d 5/2 (Te^{2-})	LA(85)	573.14	0.94	24702
		Mo-Te	3d 3/2 (Te^{2-})	LA(80)	573.53	0.92	16056
		Te-Se	3d 5/2 (Te^{δ})	LA(50)	573.46	0.95	2104
		Te-Se	3d 3/2 (Te^{δ})	LA(50)	583.86	0.73	1244
	Se 3d	Mo-Se	3d 5/2 (Te^{2-})	LA(80)	54.85	0.69	3324
		Mo-Se	3d 3/2 (Te^{2-})	LA(10)	55.68	0.86	2405
		Te-Se	3d 5/2 (Se^{δ})	LA(50)	55.27	0.90	896
		Te-Se	3d 3/2 (Se^{δ})	LA(50)	55.99	0.70	569

Calculation S1

Calculation of film stoichiometry using the relative sensitivity factor (RSF)-corrected peak areas.

The stoichiometry of the $MoTe_2$,

$$Mo{:}Te = \frac{Effective\ peak\ area\ of\ the\ (Mo-Te) component\ in\ Mo\ 3d}{Effective\ peak\ area\ of\ \ the\ (Mo-Te) component\ in\ Te\ 3d}$$

$$Mo{:}Te = \frac{Raw\ peak\ area\ of\ the\ (Mo-Te) component\ in\ Mo\ 3d \Big/ RSF\ value\ for\ Mo\ 3d}{Raw\ peak\ area\ of\ the\ (Mo-Te) component\ in\ Te\ 3d \Big/ RSF\ value\ for\ Te\ 3d}$$

For example,

Under normal emission, the Mo:Te ratio in the $MoSe_2/MoTe_2$ heterostructure (using Table S2 values),

$$Mo{:}Te = \frac{4550/3.32}{24702/9.51} = \frac{1367}{2597} = 1{:}1.90$$

Similarly, the relative percentage ratio of two different bonding states in a core level, for example, from the Te 3d spectrum in the heterostructure,

$$Te^{\delta}/Te^{2-}\ \% = \frac{2104/9.51}{24702/9.51} \times 100\ \% = 8.51\ \%$$